Thermally induced metastability of InGaAs single-layer for highly strained superlattices by metal-organic chemical vapor deposition

Sooseok Kang[a], Jongmin Kim[a], Chan Wook Jang[b], Hyunchul Jang[a], Sang Tae Lee[a], Byeong-hyeon Lee[c], Shinkeun Kim[a], Chan-Soo Shin[a], Dong-Hwan Jun[a],*

[a] *Device Engineering Labs, Korea Advanced Nano Fab Center (KANC), 109, Gwanggyo-ro, Yeongtong-gu, Suwon-si, Gyeonggi-do 16229, Republic of Korea*
[b] *Department of Applied Physics, Institute of Natural Sciences and Integrated Education Institute for Frontier Science and Technology (BK21 Four), Kyung Hee University, Yongin 17104, Republic of Korea*
[c] *Advanced Analysis Center, Korea Institute of Science and Technology (KIST), Seoul 02792, South Korea*

ARTICLE INFO

ABSTRACT

In this study, the metastability of $In_{0.68}Ga_{0.32}As$ layers on InP substrates was investigated at various growth temperatures. The thickness of each metastable $In_{0.68}Ga_{0.32}As$ layer was 40 nm, which is four times the critical thickness of the stable lattice with a stress of approximately 1%. The surface morphologies and roughness of the metastable $In_{0.68}Ga_{0.32}As$ layers were highly sensitive to the growth conditions. Cross-hatches were observed on their surfaces when they were grown at various growth temperatures, and over this range, the surface roughness varied from 0.11 nm to 0.16 nm. The lowest surface roughness of 0.11 nm was achieved at 770 °C, and the metastable $In_{0.68}Ga_{0.32}As$ layer showed a flat surface morphology with terraces parallel to the step edges. These results corresponded to those of the strain relaxation analysis of the metastable $In_{0.68}Ga_{0.32}As$ layers using X-ray diffraction spectra. The $In_{0.68}Ga_{0.32}As$ layer grown at 770 °C was almost fully strained, whereas those grown at other growth temperatures were relieved by approximately 10%. The flat surface morphologies and almost fully strained lattices suggested that the growth conditions were suitable for preparing high-quality superlattices with well-defined interfaces. The intuitive results of the metastable $In_{0.68}Ga_{0.32}As$ single layers were utilized to grow high-quality $In_{0.67}Ga_{0.33}As/Al_{0.64}In_{0.36}As$ superlattices with a reduction in the misfit dislocation by 41.8%. The results obtained herein suggest that the growth conditions for superlattices can be easily and efficiently optimized using the metastability of the materials.

© 2022 Published by Elsevier B.V.

1. Introduction

The recent advancements in novel materials, devices, and control systems have resulted in an increase in their potential because they are beneficial to human life through both the inherent properties of the materials and particularly designed device structures [1–9]. Quantum wells (QWs) have been extensively used in lasers [10], photodetectors [11], modulators [12], and solar cells [13], among other electronic devices [14]; in addition, their applications in quantum computers [2,15] and terahertz emitters [6] have attracted significant attention. QWs require a well-defined thickness and abrupt heterointerfaces without the intermixing of atoms; the latter causes a real heterointerface to deviate from an ideal flat atomic plane in two directions, i.e., along the growth (axial) direction and

in-plane of their axial positions [16]. Recently, the heterointerfaces of compound semiconductor heterostructures have shown graded composition profiles along the growth direction, which are due to the intermixing [17], segregation [18], or exchange of anions and cations, depending on the growth techniques and conditions [19]. Heterointerfaces play important roles in QWs or superlattice structures because their band structures depend largely on the hetero-interfaces. Therefore, the energy levels, wavefunction of the quantum state, and carrier transport of quantum structure devices are severely affected [17,18,20]. Moreover, for QWs or superlattices, the mismatch strain frequently results in metal surface segregation, dislocations, and their associated defects [21–24]. Therefore, it is necessary to develop a new approach for minimizing and quantifying defects for enhancing the performance of devices.

Recent studies on heterostructures have mainly reported the methods for growing superlattices that focus on controlling both the layer thickness and composition to achieve strain compensation in

the superlattices [19,22], as well as quantifying the composition modulation along the heterointerfaces at the atomic scale [17,18,25]. In the research on superlattice growth techniques, the thickness and composition of a superlattice are precisely controlled by molecular beam epitaxy [26] compared with metal–organic chemical vapor deposition (MOCVD). However, MOCVD is being increasingly used for growing superlattices [25,27] because it provides both acceptable performance of devices and high capacity for production. In addition, studies on superlattices grown by MOCVD have mainly focused on group III atoms [21,22,28,29] to quantify the atomic-scale composition modulation at their heterointerfaces. These investigations are based on the additional surface energy that can lead to a strain-induced composition modulation [21]. This type of composition modulation at heterointerfaces affects the device performance owing to the interface scattering [28,29]; therefore, the optimization of growth parameters, such as the growth temperature, growth rate, V/III ratio, and growth interruptions, has been studied [22]. However, the behavior and extent of the composition modulation associated with heterointerfaces are ambiguous, and therefore, interface roughness [29] and intermixing [17] have been investigated. Although these investigations utilized near-atomic resolution measurement techniques, such as secondary-ion mass spectrometry, transmission electron microscopy (TEM), and atom probe tomography (APT) [16,22,27], the results mainly showed some group III atom segregation, such as indium segregation [17,18]. In contrast, it was recently shown that group V atoms at heterointerfaces play an important role in modulating the composition, instead of group III atoms [30]. Moreover, the results obtained from near-atomic resolution mapping of composition through APT suggest that indium segregation is unobserved at interfaces, minimizing their artificial broadening due to surface steps or other local morphological features [31]. These conflicting findings and the artificial measurement error of a heterointerface suggest that studies on superlattices require new approaches to improve the quality of superlattices.

In most studies, high-quality superlattices were grown under various growth conditions, such as V/III ratio and growth temperatures, and subsequently characterized by different measurements, such as TEM, X-ray diffraction (XRD), atomic force microscopy (AFM), Raman spectroscopy, and photoluminescence (PL) [20,32–35]. However, the analysis of superlattices with various experimental results is complex, and an additional process, such as focus ion beam milling, is required. For example, from the XRD patterns of superlattices, it is difficult to identify the structural properties due to the Kissing fringe from their inhomogeneous layers. PL spectrum depends on various factors, such as the barrier height and the barrier/well thickness. In contrast to the superlattices, the growth and characterization of a single layer are convenient and intuitive owing to their simple structure.

However, a lattice mismatched single layer cannot be grown due to its critical thickness, which is expressed as follows:

$$h_c = \frac{1 - \sigma/4}{4\pi(1 + \sigma)} b \varepsilon_\parallel^{-1}[\ln(h_c/b) + 1],$$ (1)

where h_c and σ are the critical thickness and the dislocation Burgers vector, respectively. The theoretically expected critical thickness of a strained $In_{0.68}Ga_{0.32}As$ single layer with a lattice mismatch of approximately 1% grown on InP is approximately 10 nm. When the critical thickness is exceeded, a misfit dislocation is generated to relax the stress induced by the lattice mismatch between the single layer and substrate. Therefore, the relaxed layer does not possess structural properties similar to those of the strained layer. Below the critical thickness of 10 nm, the film is dislocation-free and is thermodynamically stable. However, analyzing the properties of a single layer is difficult because it is very thin. For example, their thinness causes the 2θ–ω signal in common XRD to be weak or unclear. In

addition, an InGaAs layer is inevitably oxidized under atmosphere conditions, and the thickness of the native oxide is approximately 2–3 nm.

Previous studies have ignored the effect of partial plastic relaxation on the crystal quality of superlattices, in which plastic relaxation [36–38] generally occurs when the critical thickness of a strained layer is exceeded. Relaxation is mediated by dislocation mechanisms [39], and changes in the dislocation density are related to the surface roughness [40]. The surface morphology evolution during epitaxial growth is known to significantly affect the efficiency of epitaxially grown quantum devices [41]. The pattern and roughness of their surfaces are related to the dislocation density of the layers grown over a rough surface [40]. Here, it should be noted that both the surface roughness and morphology can be suitable indicators for optimizing the growth conditions of metastable single layers. In addition to these indicators, because a metastable layer is unstable, it will be sensitive to the growth conditions [42,43]; therefore, its surface morphology and roughness vary significantly. However, thus far, the metastability of III–V semiconductors has not been investigated in detail.

In this study, we establish a method for the optimization of the growth conditions of a strain-balanced $In_{0.67}Ga_{0.33}As/Al_{0.64}In_{0.36}As$ superlattice utilizing the metastability of a 40-nm-thick $In_{0.67}Ga_{0.33}As$ single layer. Because a metastable layer is sensitive to the growth conditions [42,43], intuitive and helpful experimental results for the optimization of the superlattice growth were obtained. The optimized growth conditions were identified based on the experimental results, such as flat surface morphology and almost fully strained lattice of the metastable single layer. Subsequently, the misfit dislocation density of the strain-balanced $In_{0.67}Ga_{0.33}As/Al_{0.64}In_{0.36}As$ superlattice grown under the optimum growth conditions was significantly reduced.

2. Experimental

Superlattice structures for 4-μm-wavelength range quantum cascade lasers (QCLs) and single layers were grown on InP substrates (004) with off-cut angle of 0.075° using a low-pressure MOCVD system. The metal–organic sources used in the growth process were trimethylgallium, trimethylallium (TMAl), and trimethylindium (TMIn). The reactor pressure for the growth was set as 100 mbar, and the growth rate was set as under 0.3 nm/s to accurately control the thicknesses of both the single layers and superlattices. An initial target composition of InGaAs (AlInAs) was grown with near lattice matching with InP, following which two more higher indium (aluminum) compositions were grown by increasing the TMIn (TMAl) flow while maintaining the AsH$_3$ flow. Subsequently, 2θ–ω measurements were performed, and routine simulations of the compositions using the LEPTOS program were conducted. Trend lines were obtained for the InGaAs (AlInAs) composition as a function of the TMIn (TMAl) flow using the standard linear regression technique. The above procedure was repetitively performed to accurately calculate the target composition of InGaAs (AlInAs) and more importantly examine its reproducibility. The metastable single-layer indium (aluminum) composition of InGaAs (AlInAs) was chosen as 68% (63%), which presented negligible composition difference compared to that presented by the target superlattice composition [32]. The input AsH$_3$ flow (V/III ratio: 132–220) and growth temperature (Tg: 750–800 °C) were modulated to study their effects on the growth. The surface morphologies and roughness were measured via AFM (XE-100, Park Systems). The crystallographic structures were characterized by TEM (JEOL 2010 F) and XRD (d8 Discover, Bruker). First, 40-nm-thick $In_{0.68}Ga_{0.32}As$ layers are grown on InP substrates at various growth temperatures (750, 770, and 790 °C), as shown Fig. 1(a). Subsequently, superlattices, as shown in
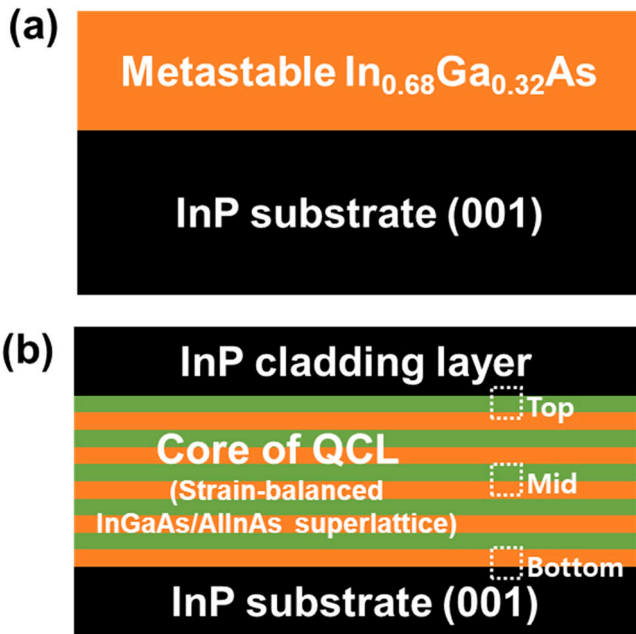
Fig. 1. (a) Schematics of metastable $In_{0.68}Ga_{0.32}As$ layers on InP substrate (001) grown at 750, 770, and 790 °C. (b) Schematic of quantum cascade laser (QCL) structure designed with InGaAs/AlInAs superlattices. It is similar to structure in reference [32]. Inverse fast Fourier transform images in Fig. 5 are obtained from dotted squares in top, mid, and bottom areas of core in QCL.

Fig. 1(b), are grown at various growth temperatures (750 and 770 °C) for comparison.

Fig. 2 shows the behavior of strained layers through theoretical or semiempirical laws for critical thickness obtained by Gendry et al. [42] and previous studies with the variation in the thickness of In-GaAs. The Matthews–Blakeslee model [44] is a well-known approach for estimating the critical thickness under thermodynamic equilibrium. However, previous studies on highly strained InGaAs layers determine their compositions by the XRD measurements and simulation of InGaAs layers with thicknesses near or below their critical thicknesses [37] and over the critical thicknesses [45], respectively. It is still ambiguous which thicknesses are important for
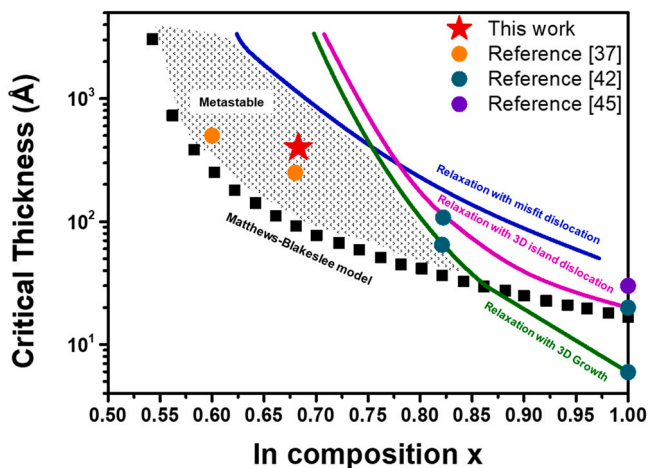

Fig. 2. Critical thickness calculated using mechanical equilibrium theory (Matthews–Blakeslee model) and thickness to relaxation of InGaAs layers with various compositions. Critical thickness is denoted by black square scatter. Blue, dark cyan, and magenta lines denote thickness for relaxation with misfit dislocation, 3D island dislocation, and 3D growth, respectively. Region between thicknesses is metastable region. Star scatter is thickness of $In_{0.68}Ga_{0.32}As$ layers in this study. Circle scatter are thicknesses of $In_xGa_{1-x}As$ layer in previous studies.

determining the InGaAs compositions and the extents of relaxation, because the possibility of partial relaxation, particularly two-dimensional relaxation, has been generally ignored and is difficult to measure using microscopic (e.g., TEM) or macroscopic (e.g., XRD) measurement methods. It has been shown that nonequilibrium leads to experimental critical thicknesses that are highly dependent on the growth conditions, particularly the growth temperature [42,45]. Consequently, metastable InGaAs layers, which are much thicker than the equilibrium critical thickness, can be obtained, and the actual thickness, at which the strain begins to be relieved, should be defined experimentally [42]. However, to the best of our knowledge, previous literature does not report the effect of the potential partial relaxation, which could mainly occur in two dimensions and over a micrometer order scale, on the crystal quality of InGaAs/AlInAs superlattices. Thus, we designed metastable 40-nm-thick $In_{0.68}Ga_{0.32}As$ layers, with average thickness of 40 nm, that lies in the middle of the metastable region in Fig. 2. Following this, the layers were grown at various growth conditions, such as growth temperature (Tg: 750–800 °C) and V/III ratio (132–220); in addition, $2\theta-\omega$ measurements were performed and routine simulations of the compositions were conducted using the LEPTOS program. Subsequently, the optimum growth conditions for a metastable 40-nm-thick $In_{0.68}Ga_{0.32}As$ layer were determined by extensively measuring and analyzing the surface morphology by AFM. Finally, the dislocation densities of highly strained $In_{0.67}Ga_{0.33}As/Al_{0.64}In_{0.36}As$ superlattices grown at 770 and 750 °C were compared, and a significantly reduced dislocation density was observed for the superlattice grown at the growth conditions for the optimum InGaAs surface morphology.

3. Results and discussion

Surface morphology with area of $5 \times 5\,\mu m$, roughness (R_q), and peak to valley (R_{pv}) of epitaxial $In_{0.68}Ga_{0.32}As$ layers on InP substrates are shown in Fig. 3. The surface morphology of an epitaxial $In_{0.68}Ga_{0.32}As$ layer grown at 750 °C is shown in Fig. 3(a). The terraces are bended, and hillocks, valleys, cusps, and cross-hatches are developed owing to the relaxation of the stress induced by the lattice mismatch between $In_{0.68}Ga_{0.32}As$ and InP. In addition, bright and dark groove belts are periodically observed, which are due to the distortion of the surface by relaxation, and the belts are formed vertically across on the surface. A cross-hatch pattern typically originates from the plastic relaxation of the stress induced by the lattice mismatch between a substrate and a film by misfit dislocations [36,46,47].

Concurrently, the surface morphology of the $In_{0.68}Ga_{0.32}As$ layer grown at 770 °C is shown in Fig. 3(b). Although the terrace interval is wider than that in Fig. 3(a), it is constant, and the terraces are parallel to each other. Lines, similar to those observed in a cross-hatch, are sporadically observed; however, the number of the lines is remarkably lesser than those noted in the other cases. This suggests that the other $In_{0.68}GaAs$ layers are more deformed by relaxation than the $In_{0.68}Ga_{0.32}As$ layer grown at 770 °C. The regular terraces suggest that the growth mode of this $In_{0.68}Ga_{0.32}As$ layer is a step-flow growth and that the relaxation of the crystal structure is minimized.

The above morphology is similar to that of the $In_{0.68}Ga_{0.32}As$ layer grown at 790 °C, as shown Fig. 3(c). The surface morphology of the latter is rougher than that of the $In_{0.68}Ga_{0.32}As$ layer grown at 750 °C. The hillocks in Fig. 3(c) are higher and the valleys are deeper than those in Fig. 3(a). In addition, a cross-hatch pattern, which is related to misfit dislocation, is shown. The abovementioned characteristics are caused by the strain of the $In_{0.68}Ga_{0.32}As$ layer induced by the lattice mismatch between the $In_{0.68}Ga_{0.32}As$ layer and InP substrate. The wider terrace compared to those of the other layers is caused by the desorption of As atoms on the surface at a higher
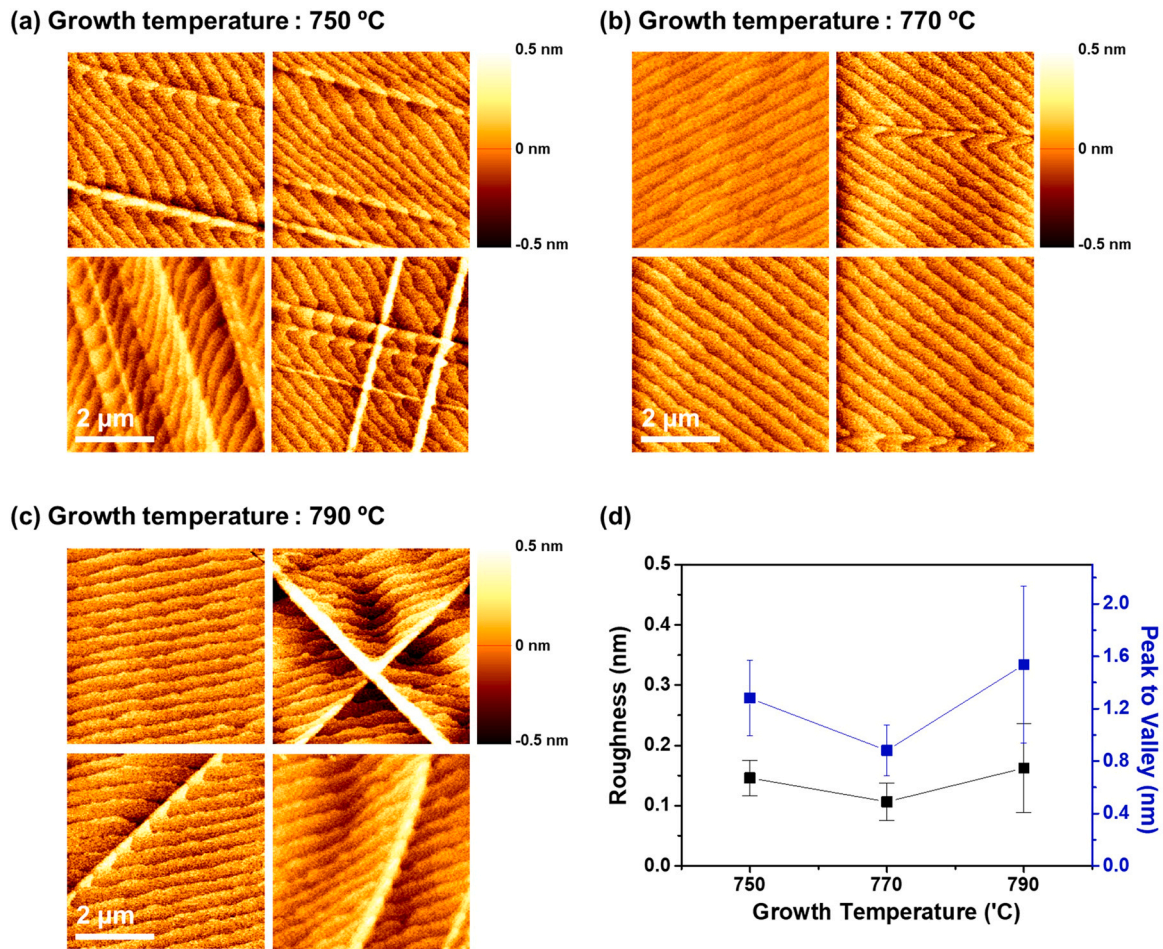
(a) Growth temperature : 750 °C

(b) Growth temperature : 770 °C

(c) Growth temperature : 790 °C

(d)

Fig. 3. Surface morphologies in (a), (b), and (c) of 40-nm-thick $In_{0.68}Ga_{0.32}As$ layers grown at 750, 770, and 790 °C, respectively. Scale bar is 2 μm. (d) Surface roughness (R_q) and peak to valley (R_{pv}) values of $In_{0.68}GaAs$ layers grown at 750, 770, and 790 °C.

growth temperature. The wider terraces suggest that the growth mode at 790 °C is a nearly step bunching growth mode [41].

The surface roughness values of the $In_{0.68}Ga_{0.32}As$ layers grown at 750, 770, and 790 °C, as shown in Fig. 3(d), are 0.146, 0.107, and 0.162 nm, respectively. Their corresponding peak to valley values are 1.28, 0.88, and 1.54 nm. The roughness and peak to valley values of the $In_{0.68}Ga_{0.32}As$ layer grown at 770 °C are the lowest among those of the three samples, and its surface is flatter than those of the other layers. This suggests that the $In_{0.68}Ga_{0.32}As$ layer grown at 770 °C is less deformed and its critical thickness for relaxation is thicker than those of the others [42].

The structural properties of the $In_{0.68}GaAs$ layers grown at the various growth temperatures are shown in Fig. 4. The XRD 2θ–ω scans were measured and plotted. The scatter plots were fitted by the LEPTOS software. The peak 2θ angles of the $In_{0.68}Ga_{0.32}As$ layers grown at 750, 770, and 790 °C are 61.949°, 61.885°, and 69.962°, respectively. Remarkably, the 2θ angles are smaller than the 2θ angle for a fully relaxed $In_{0.68}Ga_{0.32}As$ layer (62.625°). This suggests that the cubic lattices of the $In_{0.68}Ga_{0.32}As$ layers are partially strained and that the cubic structures are metastable. Although the three $In_{0.68}Ga_{0.32}As$ layers are partially strained, the peak angles of the layers grown at 750 and 790 °C are higher than that of the $In_{0.68}Ga_{0.32}As$ layer grown at 770 °C. This difference in the peak angles is attributed to relaxation in the layers. The abovementioned XRD results are consistent with the AFM results, as shown in Fig. 3. The two $In_{0.68}Ga_{0.32}As$ layers grown at 750 and 790 °C are relieved owing to the plastic deformation of the crystal structures, as shown in Fig. 3. The relaxation of the both layers along out of plane is 10%
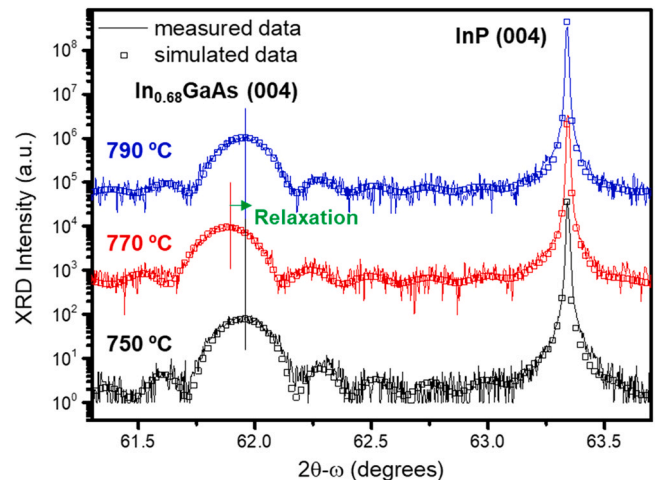

Fig. 4. Measured and fitted XRD 2θ–ω scan spectra of $In_{0.68}Ga_{0.32}As$ layers grown at various growth temperatures. Line plot shows measured data, and scatter plot shows simulated data.

higher than that of the $In_{0.68}Ga_{0.32}As$ layer grown at 770 °C, and it is calculated using an XRD simulation software. Based on the results of reciprocal space mapping with direction [224] (not shown here), the $In_{0.68}Ga_{0.32}As$ layers grown at 750, 770, and 790 °C are relaxed along the azimuthal direction by 0.87%, 0.1%, and 0.67%, respectively.
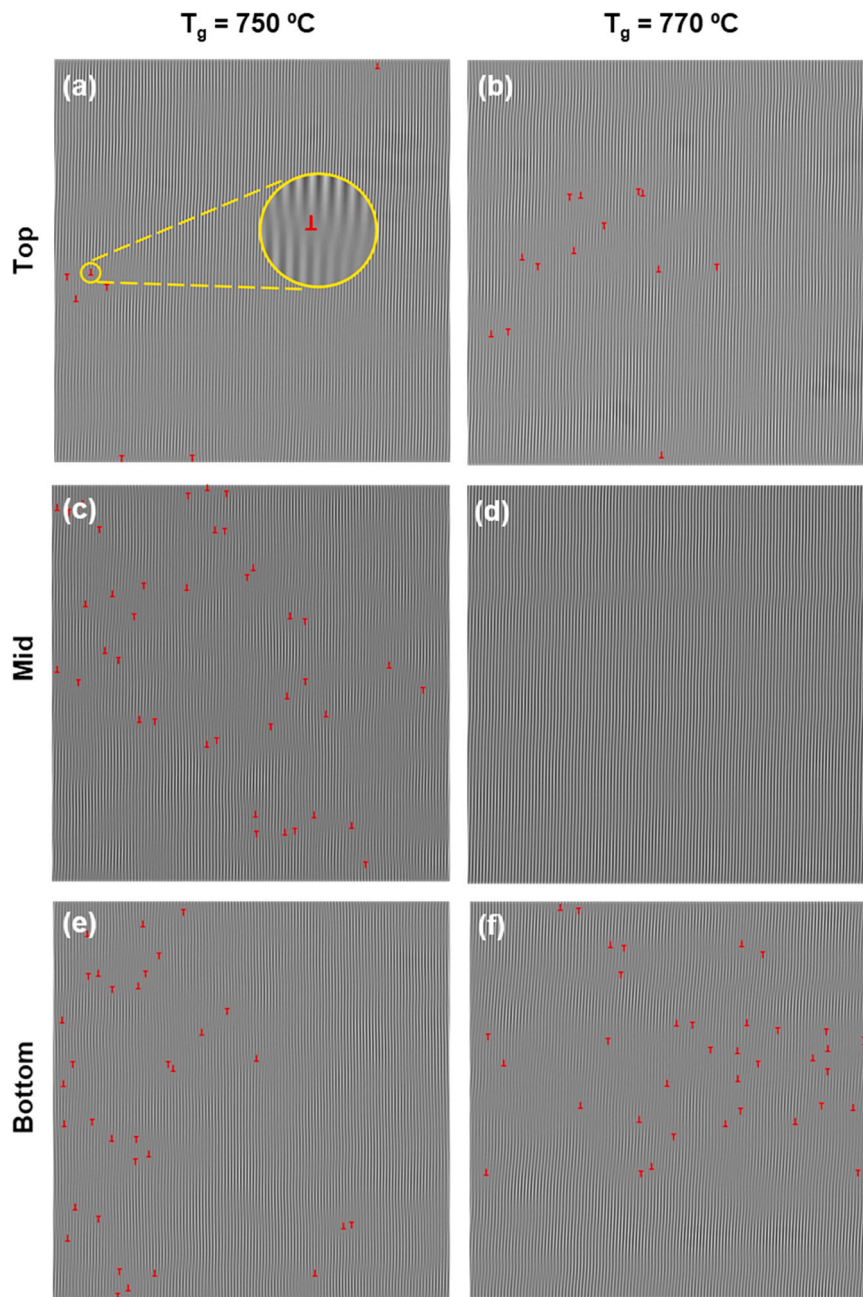
Fig. 5. (a), (c), and (e) are inverse fast Fourier transform (FFT) images of top, mid, and bottom areas in core layer grown at 750 °C, respectively. (b), (d), and (f) are inverse FFT images of top, mid, and bottom areas in core layer grown at 770 °C, respectively. Misfit dislocations are indicated by red ⊤ and ⊥ markers in inverse FFT images.

The misfit dislocations can be easily identified from the inverse fast Fourier transform (FFT) images shown in Fig. 5. The inverse FFT images of the QCLs grown at 750 and 770 °C are shown in Fig. 5(a), (c), (e) and (b), (d), (f), respectively. Fig. 5(a) and (b) show the inverse FFT images of the top layers in the cores grown at 750 and 770 °C, respectively. The misfit dislocations are indicated by red marker shown in a yellow circle in Fig. 5(a). A total of 7 and 13 misfit dislocations are counted in the top layers grown at 750 and 770 °C, respectively. The inverse FFT images of the mid layers of the core grown at 750 and 770 °C are shown in Fig. 5(c) and (d), respectively. A total of 39 misfit dislocations are identified in the mid layers grown at 750 °C, whereas no misfit dislocation exists in those grown at 770 °C. A total of 40 and 37 misfit dislocations are generated in the bottom of the cores grown at 750 and 770 °C, respectively. The bottom of a core is exposed to heating during the growth of the QCL layers. Thus, the generation of many misfit dislocations in the

bottom area is attributed to the annealing effect of the growth temperature. A total of 86 and 50 misfit dislocations are counted in the QCLs grown at 750 and 770 °C, respectively. Misfit dislocations are reduced by 41.8% in the core of the QCL grown at 770 °C compared to those in the former. This relaxation by the generation of misfit dislocations is in agreement with the results of AFM, as shown in Fig. 3.

Most of the literature on the growth of superlattices reported experimental and theoretical results of superlattices grown under various growth condition and followed by the explanation of the optimization of a growth condition. However, it is difficult to analyze the results obtained from superlattices owing to their complexity. In contrast to previous research, in this study, the growth conditions for superlattices are optimized with a metastable InGaAs single layer. The analysis of a single layer provides a rapid and intuitive method to determine the properties of superlattices.

4. Conclusions

In this study, the metastability of strained $In_{0.68}Ga_{0.32}As$ single layers grown at the various growth temperature was investigated. Although the thickness of each $In_{0.68}Ga_{0.32}As$ layer was 40 nm, which is four times the critical thickness (10 nm), the optimized $In_{0.68}Ga_{0.32}As$ layer is almost fully strained and shows a flat surface with regular terraces. Using the optimized growth condition of the 40-nm-thick metastable $In_{0.68}Ga_{0.32}As$ layers, the misfit dislocation density of the corresponding highly strained $In_{0.67}Ga_{0.33}As$/$Al_{0.64}In_{0.36}As$ superlattice for a 4-μm-wavelength range QCL was reduced by 41.8% compared to that of the unoptimized growth condition superlattice. Therefore, optimizing the growth conditions of metastable single layers could be an effective method to optimize the growth conditions of strain-balanced superlattices. This because the experimental results obtained from the metastable samples are more intuitive and helpful than those obtained from superlattices or a single layer of thickness under the critical thickness. The experimental results from a superlattice are complex to analyze and those from a single layer of thickness over or under the critical thickness frequently mislead the critical material information, such as composition. We believe that the growth conditions for strained or strain-balanced superlattices consisting can be conveniently optimized using the metastability of the materials. In future, we will investigate the metastability of InGaAs and AlInAs layers with various compositions and thicknesses.

CRediT authorship contribution statement

Sooseok Kang: Conceptualization, Validation, Visualization, Writing – original draft. **Jongmin Kim:** Writing – review & editing, Validation. **Chan Wook Jang:** Writing – review & editing, Validation. **Hyunchul Jang:** Writing – review & editing. **Sang Tae Lee:** Writing – review & editing. **Byeong-hyeon Lee:** Investigation, Resources. **Shinkeun Kim:** Writing – review & editing, Resources. **Chan-Soo Shin:** Writing – review & editing, Resources. **Dong-Hwan Jun:** Writing – original draft, Visualization, Supervision, Project administration.

Declaration of Competing Interest

The authors declare the following financial interests/personal relationships which may be considered as potential competing interests: Dong-Hwan Jun reports financial support was provided by National Research Foundation of Korea.

Acknowledgments

References

[1] G. Xia, Y. Huang, F. Li, L. Wang, J. Pang, L. Li, K. Wang, A thermally flexible and multi-site tactile sensor for remote 3D dynamic sensing imaging, Front. Chem. Sci. Eng. 14 (2020) 1039–1051, https://doi.org/10.1007/s11705-019-1901-5

[2] M.C. Dartiailh, J.J. Cuozzo, B.H. Elfeky, W. Mayer, J. Yuan, K.S. Wickramasinghe, E. Rossi, J. Shabani, Missing Shapiro steps in topologically trivial Josephson junction on InAs quantum well, Nat. Commun. 12 (2021), https://doi.org/10.1038/s41467-020-20382-y

[3] X. Feng, Y. Zhang, L. Kang, L. Wang, C. Duan, K. Yin, J. Pang, K. Wang, Integrated energy storage system based on triboelectric nanogenerator in electronic devices, Front. Chem. Sci. Eng. 15 (2021) 238–250, https://doi.org/10.1007/s11705-020-1956-3

[4] C. Bu, F. Li, K. Yin, J. Pang, L. Wang, K. Wang, Research progress and prospect of triboelectric nanogenerators as self-powered human body sensors, ACS Appl. Electron. Mater. 2 (2020) 863–878, https://doi.org/10.1021/acsaelm.0c00022

[5] X. Feng, Q. Li, K. Wang, Waste plastic triboelectric nanogenerators using recycled plastic bags for power generation, ACS Appl. Mater. Interfaces 13 (2021) 400–410, https://doi.org/10.1021/acsami.0c16489

[6] F.P. Mezzapesa, L. Viti, L. Li, V. Pistore, S. Dhillon, A.G. Davies, E.H. Linfield, M.S. Vitiello, Chip-scale Terahertz frequency combs through integrated inter-subband polariton bleaching, Laser Photonics Rev. 15 (2021), https://doi.org/10.1002/lpor.202000575

[7] J. Zhao, F. Li, Z. Wang, P. Dong, G. Xia, K. Wang, Flexible PVDF nanogenerator-driven motion sensors for human body motion energy tracking and monitoring, J. Mater. Sci. Mater. Electron. 32 (2021) 14715–14727, https://doi.org/10.1007/s10854-021-06027-w

[8] Y. Hua, N. Wang, K. Zhao, Simultaneous unknown input and state estimation for the linear system with a rank-deficient distribution matrix, Math. Probl. Eng. (2021) (2021), https://doi.org/10.1155/2021/6693690

[9] C. Liu, Q. Li, K. Wang, State-of-charge estimation and remaining useful life prediction of supercapacitors, Renew. Sustain. Energy Rev. 150 (2021) 111408, https://doi.org/10.1016/j.rser.2021.111408

[10] J.G. Coutard, M. Brun, M. Fournier, O. Lartigue, F. Fedeli, G. Maisons, J.M. Fedeli, S. Nicoletti, M. Carras, L. Duraffourg, Volume fabrication of quantum cascade lasers on 200 mm-CMOS pilot line, Sci. Rep. 10 (2020) 1–8, https://doi.org/10.1038/s41598-020-63106-4

[11] Y. Zhu, S. Zhai, J. Liu, Kun Li, K. Yang, S. Liu, Jinchuan Zhang, N. Zhuo, Lijun Wang, F. Liu, Mid-wave/long-wave dual-color infrared quantum cascade detector enhanced by antenna-coupled microcavity: erratum, Opt. Express 29 (2021) 37327–37335, https://doi.org/10.1364/oe.448016

[12] H. Kamada, T. Arakawa, Proposal of highly efficient quantum well microring resonator-loaded optical phase modulator integrated with antenna-coupled electrodes for radio-over-fiber, Photonics 8 (2021) 1–14, https://doi.org/10.3390/photonics8020037

[13] D.K. Ferry S.M. Goodnick I.R. Sellers V.R. Whiteside. Valley photovoltaics and the search for the hot carrier solar cell, in: Conf. Rec. IEEE Photovolt. Spec. Conf. 2020-June 2020 0498 0501 ⟨https://doi.org/10.1109/PVSC45281.2020.9300499⟩.

[14] S.T. Lee, I.G. Lee, H. Jang, M. Kong, C. Song, C.Z. Kim, S.H. Jung, Y. Choi, S. Kim, S. keun Eom, K. seok Seo, D.H. Kim, D.H. Ko, C.S. Shin, High performance InGaAs channel MOSFETs on highly resistive InAlAs buffer layers, Solid. State Electron. 176 (2021) 107940, https://doi.org/10.1016/j.sse.2020.107940

[15] K. Sardashti, M.C. Dartiailh, J. Yuan, S. Hart, P. Gumann, J. Shabani, Voltage-tunable superconducting resonators: a platform for random access quantum memory, IEEE Trans. Quantum Eng. 1 (2021) 1–7, https://doi.org/10.1109/tqe.2020.3034553

[16] T. Grange, S. Mukherjee, G. Capellini, M. Montanari, L. Persichetti, L. Di Gaspare, S. Birner, A. Attiaoui, O. Moutanabbir, M. Virgilio, M. De Seta, Atomic-scale insights into semiconductor heterostructures: from experimental three-dimensional analysis of the interface to a generalized theory of interfacial roughness scattering, Phys. Rev. Appl. 13 (2020) 1, https://doi.org/10.1103/PhysRevApplied.13.044062

[17] X. Chai, R. Guzman, Y. Zhou, Z. Xu, Z. Liang, Y. Zhu, W. Zhou, Y. Zhou, Interfacial intermixing and its impact on the energy band structure in interband cascade infrared photodetectors, ACS Appl. Mater. Interfaces 13 (2021) 38553–38560, https://doi.org/10.1021/acsami.1c02463

[18] Y. Maidaniuk, R. Kumar, Y.I. Mazur, A.V. Kuchuk, M. Benamara, P.M. Lytvyn, G.J. Salamo, Indium segregation in ultra-thin In(Ga)As/GaAs single quantum wells revealed by photoluminescence spectroscopy, Appl. Phys. Lett. 118 (2021), https://doi.org/10.1063/5.0039107

[19] P. Mishra, R.K. Pandey, S. Kumari, A. Pandey, S. Dalal, R. Sankarasubramanian, S. Channagiri, S.K. Jangir, R. Raman, T. Srinivasan, D.V.S. Rao, Interface engineered MBE grown InAs/GaSb based type-II superlattice heterostructures, J. Alloy. Compd. 889 (2022) 161692, https://doi.org/10.1016/j.jallcom.2021.161692

[20] A. Łozińska, M. Badura, J. Jadczak, K. Bielak, B. Ściana, Photoluminescence and Raman spectroscopies as an optical approach of stress determining in MOVPE grown quantum cascade laser structures, Opt. Appl. 50 (2020) 289–299, https://doi.org/10.37190/OA200212

[21] Z. Lv, H. Wang, H. Jiang, Surface evolution of thick InGaN epilayers with growth interruption time, J. Phys. Chem. C 125 (2021) 16643–16651, https://doi.org/10.1021/acs.jpcc.0c11414

[22] A.E. Yachmenev, S.S. Pushkarev, R.R. Reznik, R.A. Khabibullin, D.S. Ponomarev, Arsenides-and related III-V materials-based multilayered structures for terahertz applications: various designs and growth technology, Prog. Cryst. Growth Charact. Mater. 66 (2020) 100485, https://doi.org/10.1016/j.pcrysgrow.2020.100485

[23] M. Sawicka, J. Smalc-Koziorowska, M. Kryśko, N. Fiuczek, P. Wolny, A. Feduniewicz-Żmuda, K. Nowakowski-Szkudlarek, H. Turski, C. Skierbiszewski, Composition inhomogeneity in nonpolar (101⁻ 0) and semipolar (202⁻ 1) InAlN layers grown by plasma-assisted molecular beam epitaxy, Cryst. Growth Des. 21 (2021) 5223–5230, https://doi.org/10.1021/acs.cgd.1c00560

[24] B. Zhang, H. Wang, X. Wang, Q. Wang, J. Fan, Y. Zou, X. Ma, Effect of GaAs insertion layer on the properties improvement of InGaAs/AlGaAs multiple quantum wells grown by metal-organic chemical vapor deposition, J. Alloy. Compd. 872 (2021) 159470, https://doi.org/10.1016/J.JALLCOM.2021.159470

[25] Q. Yang, R. Yuan, L. Wang, R. Shi, J.M. Zuo, Antimony segregation in an InAs/InAs1−xSbx superlattice grown by metalorganic chemical vapor deposition, J. Appl. Phys. 130 (2021), https://doi.org/10.1063/5.0060777

[26] H. Wang, J. Zhang, F. Cheng, N. Zhuo, S. Zhai, J. Liu, L. Wang, S. Liu, F. Liu, Z. Wang, Watt-level, high wall plug efficiency, continuous-wave room temperature quantum cascade laser emitting at 77μm, Opt. Express 28 (2020) 40155, https://doi.org/10.1364/oe.412943

[27] B. Knipfer, A. Rajeev, D. Isheim, J.D. Kirch, S.E. Babcock, T.F. Kuech, T. Earles, D. Botez, L.J. Mawst, Layer-thickness dependence of the compositions in strained III–V superlattices by atom probe tomography, J. Cryst. Growth 535 (2020) 125550, https://doi.org/10.1016/j.jcrysgro.2020.125550

[28] K.M. Oresick, J.D. Kirch, L.J. Mawst, D. Botez, Highly efficient ~8 μ m-emitting, step-taper active-region quantum cascade lasers, AIP Adv. 11 (2021), https://doi.org/10.1063/5.0037761

[29] T. Fei, S. Zhai, J. Zhang, N. Zhuo, J. Liu, L. Wang, S. Liu, Z. Jia, K. Li, Y. Sun, K. Guo, F. Liu, Z. Wang, High power λ ~ 8.5 μm quantum cascade laser grown by MOCVD operating continuous-wave up to 408 K, J. Semicond. 42 (2021), https://doi.org/10.1088/1674-4926/42/11/112301

[30] Y. Wu, Y. Zhang, Y. Zhao, C. Cai, Y. Zhang, Y. Zhang, C. Liang, Y. Xu, Z. Niu, Y. Shi, R. Che, Insights into growth-oriented interfacial modulation within semiconductor multilayers, ACS Appl. Mater. Interfaces 13 (2021) 27262–27269, https://doi.org/10.1021/acsami.1c04077

[31] A. Rajeev, W. Chen, J.D. Kirch, S.E. Babcock, T.F. Kuech, T. Earles, L.J. Mawst, Interfacial mixing analysis for strained layer superlattices by atom probe tomography, Crystals 8 (2018) 1–9, https://doi.org/10.3390/cryst8110437

[32] P. Gutowski, I. Sankowska, P. Karbownik, D. Pierścińska, O. Serebrennikova, M. Morawiec, E. Pruszyńska-Karbownik, K. Gołaszewska-Malec, K. Pierściński, J. Muszalski, M. Bugajski, MBE growth of strain-compensated InGaAs/InAlAs/InP quantum cascade lasers, J. Cryst. Growth 466 (2017) 22–29, https://doi.org/10.1016/j.jcrysgro.2017.02.031

[33] Y. Huang, J.H. Ryou, R.D. Dupuis, C. Pflgl, F. Capasso, K. Sun, A.M. Fischer, F.A. Ponce, Optimization of growth conditions for InGaAs/InAlAs/InP quantum cascade lasers by metalorganic chemical vapor deposition, J. Cryst. Growth 316 (2011) 75–80, https://doi.org/10.1016/j.jcrysgro.2010.12.028

[34] H. Dong, J. Sun, S. Ma, J. Liang, T. Lu, Z. Jia, X. Liu, B. Xu, Effect of potential barrier height on the carrier transport in InGaAs/GaAsP multi-quantum wells and photoelectric properties of laser diode, Phys. Chem. Chem. Phys. 18 (2016) 6901–6912, https://doi.org/10.1039/c5cp07805a

[35] D.H. Kim, H.Y. Jeong, Y.S. Choi, D. Park, Y.-J. Jeon, D.-H. Jun, InGaAs/InAlAs quantum cascade lasers grown by using metal-organic vapor-phase epitaxy, Appl. Sci. Converg. Technol. 26 (2017) 139–142, https://doi.org/10.5757/asct.2017.26.5.139

[36] Y.B. Bolkhovityanov, A.S. Deryabin, A.K. Gutakovskii, M.A. Revenko, L.V. Sokolov, Dominating nucleation of misfit dislocations from the surface in GeSi/Si(0 0 1) films with a stepwise composition grown by means of molecular-beam epitaxy, J. Cryst. Growth 293 (2006) 247–252, https://doi.org/10.1016/j.jcrysgro.2006.05.018

[37] J.C. Shin, L.J. Mawst, D. Botez, Crystal growth via metal-organic vapor phase epitaxy of quantum-cascade-laser structures composed of multiple alloy compositions, J. Cryst. Growth 357 (2012) 15–19, https://doi.org/10.1016/j.jcrysgro.2012.07.013

[38] B. Smiri, M. Ben Arbia, D. Ilkay, F. Saidi, Z. Othmen, B. Dkhil, A. Ismail, E. Sezai, F. Hassen, H. Maaref, Optical and structural properties of In-rich InxGa1−xAs epitaxial layers on (1 0 0) InP for SWIR detectors, Mater. Sci. Eng. B Solid-State Mater. Adv. Technol. 262 (2020) 114769, https://doi.org/10.1016/j.mseb.2020.114769

[39] M.S. Colla, B. Amin-Ahmadi, H. Idrissi, L. Malet, S. Godet, J.P. Raskin, D. Schryvers, T. Pardoen, Dislocation-mediated relaxation in nanograined columnar palladium films revealed by on-chip time-resolved HRTEM testing, Nat. Commun. 6 (2015) 2–9, https://doi.org/10.1038/ncomms6922

[40] D.P. Masson, S. Laframboise, Surface roughness and dislocation density in InP/InGaAs, Photonics North 2004 Opt. Compon. Devices 5577 (2004) 74, https://doi.org/10.1117/12.567540

[41] K. Bellmann, U.W. Pohl, C. Kuhn, T. Wernicke, M. Kneissl, Controlling the morphology transition between step-flow growth and step-bunching growth, J. Cryst. Growth 478 (2017) 187–192, https://doi.org/10.1016/j.jcrysgro.2017.09.007

[42] M. Gendry, V. Drouot, C. Santinelli, G. Hollinger, Critical thicknesses of highly strained InGaAs layers grown on InP by molecular beam epitaxy, Appl. Phys. Lett. 60 (1992) 2249–2251, https://doi.org/10.1063/1.107045

[43] J.W. Lv, C. Wei, S. Zhang, Z.L. Shi, H.R. Zhang, X.Y. Zhang, M.Z. Ma, Microstructure and Mechanical behavior evolution of Ti-based bulk metallic glass induced by sub-T isothermal annealing, J. Alloy. Compd. 900 (2022) 163300, https://doi.org/10.1016/j.jallcom.2021.163300

[44] J.W. Matthews, A.E. Blakeslee, Defects in epitaxial multilayers, J. Cryst. Growth 27 (1974) 118–125, https://doi.org/10.1007/978-3-319-11863-5_8

[45] H. Sugiyama, T. Hoshi, H. Yokoyama, H. Matsuzaki, Metal-organic vapor-phase epitaxy growth of InP-based HEMT structures with InGaAs/InAs composite channel, in: Conf. Proc. - Int. Conf. Indium Phosphide Relat. Mater., 2012, pp. 245–248. ⟨https://doi.org/10.1109/ICIPRM.2012.6403369⟩.

[46] A.M. Andrews, J.S. Speck, A.E. Romanov, M. Bobeth, W. Pompe, Modeling crosshatch surface morphology in growing mismatched layers, J. Appl. Phys. 91 (2002) 1933–1943, https://doi.org/10.1063/1.1428091

[47] A.M. Andrews, R. LeSar, M.A. Kerner, J.S. Speck, A.E. Romanov, A.L. Kolesnikova, M. Bobeth, W. Pompe, Modeling crosshatch surface morphology in growing mismatched layers. Part II: periodic boundary conditions and dislocation groups, J. Appl. Phys. 95 (2004) 6032–6047, https://doi.org/10.1063/1.1707208